PCCP

Novel insights into lattice thermal transport in nanocrystalline Mg3Sb2 from first principles: The crucial role of higher-order phonon scattering

Journal:	*Physical Chemistry Chemical Physics*
Manuscript ID	CP-ART-04-2022-001967.R1
Article Type:	Paper
Date Submitted by the Author:	27-Jun-2022
Complete List of Authors:	Chang, Zheng; Dalian University of Technology, School of Energy and Power Engineering Zheng, Jiongzhi; The Hong Kong University of Science and Technology, Mechanical and Aerospace Engineering Jing, Yuhang; Harbin Institute of Technology, Department of Astronautical Science and Mechanics Li, Weiqi; Harbin Institute of Technology, Physics Yuan, Kunpeng; Dalian University of Technology, Ma, Jing; Dalian University of Technology, School of Energy and Power Engineering Gao, Yufei; Dalian University of Technology, School of Energy and Power Engineering Zhang, Xiaoliang; Dalian University of Technology, School of Energy and Power Engineering Hu, Ming; University of South Carolina, Mechanical Engineering yang, jianqun; Harbin Institute of Technology, School of Materials Science and Engineering Tang, Dawei; Dalian University of Technology, School of Energy and Power Engineering

Novel insights into lattice thermal transport in nanocrystalline Mg_3Sb_2 from first principles: The crucial role of higher-order phonon scattering

Zheng Chang[a,‡], Jiongzhi Zheng[b,‡], Yuhang Jing[e], Weiqi Li[f], Kunpeng Yuan[a], Jing Ma[a], Yufei Gao[a], Xiaoliang Zhang[a,*], Ming Hu[c,*], Jianqun Yang[d,*], Dawei Tang[a,*]

[a]*Key Laboratory of Ocean Energy Utilization and Energy Conservation of Ministry of Education, School of Energy and Power Engineering, Dalian University of Technology, Dalian 116024, China.*

[b]*Department of Mechanical and Aerospace Engineering, The Hong Kong University of Science and Technology, Clear Water Bay, Kowloon, Hong Kong 999077, China.*

[c]*Department of Mechanical Engineering, University of South Carolina, Columbia, South Carolina 29208, USA.*

[d]*School of Materials Science and Engineering, Harbin Institute of Technology, Harbin 150001, China*

[e]*School of Astronautics, Harbin Institute of Technology, Harbin 150001, China*

[f]*School of Physics, Harbin Institute of Technology, Harbin 150001, China*

[*]*Corresponding author. Email: zhangxiaoliang@dlut.edu.cn, hu@sc.edu, yangjianqun@hit.edu.cn and dwtang@dlut.edu.cn*

‡These authors contributed equally.

Abstract

Zintl phase Mg_3Sb_2, which has ultra-low thermal conductivity, is a promising anisotropic thermoelectric material. It is worth noting that the prediction and experiment value of lattice thermal conductivity (κ) maintain a remarkable difference, troubling the development and application. Thus, we firstly included the four-phonon scattering processes effect and performed the Peierls-Boltzmann transport equation (PBTE) combined with the first-principles lattice dynamics to study the lattice thermal transport in Mg_3Sb_2. The results showed that our theoretically predicted κ is consistent with the experimentally measured, breaking through the limitations of the traditional calculation methods. The prominent four-phonon scatterings decreased phonon lifetime, leading to the κ of Mg_3Sb_2 at 300 K from 2.45 (2.58) $Wm^{-1}K^{-1}$ to 1.94 (2.19) $Wm^{-1}K^{-1}$ along the in (cross)-plane directions, respectively, and calculation accuracy increased by 20%. This study successfully explains the lattice thermal transport behind mechanism in Mg_3Sb_2 and implies guidance to advance the prediction accuracy of thermoelectric materials.

***Keywords**:* Zintl phase Mg_3Sb_2; Ultra-low thermal conductivity; Promising thermoelectric materials; Non-diagonal term; Four-phonon scattering

1. **Introduction**

In the global energy field, the electricity from coal combustion was about 34%[1], which is worthy to attention and suppressed the CO_2 emission from the thermal power process. Furthermore, the electrically-driven systems generate large amounts of waste heat in industrial processes, resulting in the utilization of electricity inadequate. Thus, the use of efficient thermoelectric materials (TEs) is a direct way to reuse waste heat and reduce carbon emissions[2]. The energy conversion efficiency of TEs can be evaluated by the dimensionless figure of merit[3-5]: $ZT = \sigma S^2 T / \kappa_{Total}$, where σ, S, T

and κ_{Total} represent the electrical conductivity, Seebeck coefficient, Kelvin temperature and total thermal conductivity, respectively. Recently, the Mg_3Sb_2 compound, which is regarded as a prototype of a family of so-called Zintl phase, has attracted intensive attention and has driven a great effort to tune the electrical and lattice thermal transport properties[6-9]. On the one hand, the Mg_3Sb_2 crystal possesses superior electronic properties, namely, an intrinsic multivalley conduction band manifold, and its bandgap can be easily tuned by alloying[10-12]. On the other hand, the anomalously low lattice thermal conductivity (κ) of nanocrystalline Mg_3Sb_2 was observed in experiments[13, 14], resulting from weak and anharmonic chemical bonding of Mg-Sb pair and the undersized Mg cation[15, 16]. These two factors contribute to the high ZT of n-type Mg_3Sb_2, *i.e.*, 1.6 at 720 K[17], and make it applicable in thermoelectrics. However, the predicted and experimental test value of the κ indicated the disparity, suffering the utilization and optimization of Mg_3Sb_2. Hence, accurate computing the thermoelectric transport parameters is the main challenge to breaking through Mg_3Sb_2 performance.

To unveil lattice thermal transport mechanisms behind the unusually low κ in nanocrystalline Mg_3Sb_2, Maccioni *et al.*[18] computed the lattice thermal conductivity of Mg_3Sb_2 crystal from the first principles calculations considering three-, isotope-, and boundary-phonon scatterings. However, they reported a relatively high κ, *i.e.*, over 10 $Wm^{-1}K^{-1}$, at 300 K and attributed the low experimental κ to the grain-boundary scattering of phonons. Conversely, Zhang *et al.*[11] reported a much lower and nearly isotropic thermal conductivity around 1.2 $Wm^{-1}K^{-1}$ at 300 K based on the first-principle-based PBTE considering only three-phonon scattering. Using the same method, Meng *et al.*[19] presented the anisotropic thermal conductivity of Mg_3Sb_2 crystal with values of 1.85 and 1.93 $Wm^{-1}K^{-1}$ at the same temperature along in- and out of-plane directions, respectively. Considering the strong anharmonic chemical bonding in nanocrystalline Mg_3Sb_2, Zhu *et al.*[20] used a temperature-dependent effective potential (TDEP)[21, 22] approach to account for the temperature effect on lattice thermal transport and explained the unconventional temperature dependence of thermal conductivity in Mg_3Sb_2. Despite

significant theoretical efforts, the conventional PBTE method considering only three-phonon scattering processes was found to be insufficient to explain the experimentally measured low κ in nanocrystalline Mg_3Sb_2[13, 14].

Inspired by the shortcoming of the conventional PBTE method in describing the thermal transport, we develop a comprehensive theoretical understanding of lattice thermal transport in nanocrystalline Mg_3Sb_2 using a direct state-of-the-art first-principles-based PBTE method. The lattice thermal transport theory including the effects of three-, four-, isotope-, and boundary-phonon scatterings processes were tested for nanocrystalline Mg_3Sb_2 in this work. Furthermore, we explicitly compute the coherence contributions from the off-diagonal terms of heat flux operator, which dominates thermal transport in materials with ultra-low κ and strong phonon anharmonicity[23-26]. We find that four-phonon (4ph) scattering processes play a crucial role in determining the κ, thereby resulting in the improved agreement with experiments. The lattice thermal transport contributed by off-diagonal terms of heat flux operators is of minor importance and can be neglected, revealing the dominant role of phonon nature in nanocrystalline Mg_3Sb_2. In contrast to the previous work[18] highlighting the important role of the boundary scattering in resolving the discrepancies between the predicted and experimental κ, our results mainly attribute the corresponding discrepancies to the effect of 4ph scatterings and reveal the microscopic mechanism of higher-order phonon scattering processes in Mg_3Sb_2.

2. **Computational details and methodology**

2.1 **Density functional theory calculations**

In this study, all the density-functional-theory (DFT) calculations [27] were performed with the Vienna *Ab-initio* Simulation Package (VASP)[28, 29], where the projector-augmented wave (PAW)[30] pseudopotentials were used to treat Mg ($3s^2$) and Sb ($5s^2$ $5p^3$) shells as valence states. For the

exchange-correlation functional, we used the generalized gradient approximation (GGA) in the form of the Perdew–Burke–Ernzerhof revised for solids (PBEsol)[31, 32]. The unit-cell structural optimization of Mg_3Sb_2 crystal was performed on a five-atoms primitive cell employing an $8\times8\times6$ Monkhorst-Pack *k*-point grids to sample the Brillouin zone (BZ). All the calculations were performed using a plane-wave basis set of 500 eV for the BZ integration. The structure relaxation calculations used a tight convergence threshold of 10^{-5} eV·Å^{-1} for forces, and 10^{-8} eV for the total energy.

The harmonic and anharmonic interatomic force constants (IFCs), namely, the 2nd, 3rd, and 4th order force constants, were required as input in solving the PBTE[33, 34]. We first fit the 2nd and 3rd order force constants using the finite-temperature method, as implemented in the TDEP[21, 22], where the trajectories of the *ab-initio* molecular dynamics (AIMD) simulation for Mg_3Sb_2 crystal were needed. The AIMD simulation used a 4×4×2 supercell containing 160 atoms with the Γ-point for the Brillouin-zone integration and a convergence threshold of 10^{-5} eV for the electronic self-consistent field cycles. Additionally, we ran the AIMD simulation in the NVT ensemble using a Nosé Hoover thermostat to control temperature and the simulation trajectories were 20 ps long with a time step of 2 fs. To this end, a default value in the TDEP method was set as the cutoff radius for the 2nd order IFCs and a cutoff radius of 5.5 Å was used for the 3rd order IFCs. To further account for 4ph interaction processes in solving PBTE, we used the compressive sensing lattice dynamics method (CSLD)[35] to extract the higher-order force constants, namely, 4th order force constants, based on a limited dataset. We first sampled 160 uncorrelated configurations from the above AIMD simulation trajectories and further displaced all atoms of all configurations by 0.1 Å in random directions. After that, we recalculated all configurations using a 3×3×3 *k*-point grid to achieve the desired accuracy. To this end, we already obtained all interatomic force constants including 2nd, 3rd, and 4th order force constants.

2.2. **Lattice thermal conductivity calculations**

Using the above obtained IFCs, the κ can be calculated by solving the PBTE for the nonequilibrium distribution function iteratively, as implemented in ShengBTE and FourPhonon packages[36, 37]. Herein, the general form of the linearized PBTE considering three- and four-phonon scattering processes was given as[38-40]:

$$\boldsymbol{F}_\lambda = \tau_\lambda^0 \left(\boldsymbol{v}_\lambda + \boldsymbol{\Delta}_\lambda \right), \tag{1}$$

where λ represents a shorthand notation of phonon mode $(\boldsymbol{q}, j)$ ($\boldsymbol{q}, j$ denote sampled phonon wavevector and phonon band, respectively), $\boldsymbol{v}_\lambda$ represents the intraband group velocity associated with phonon mode λ, $\boldsymbol{\Delta}_\lambda$ represents the correction term under the single-mode relaxation time approximation (SMRTA), which includes isotope-, three-, and four-phonon scattering, and it can be explicitly written as:

$$\begin{aligned}
\boldsymbol{\Delta}_\lambda = & \frac{1}{N_0} \sum_{\lambda' \lambda''}^{(+)} \Gamma_{\lambda\lambda'\lambda''}^{(+)} \left(\xi_{\lambda\lambda''} F_{\lambda''} - \xi_{\lambda\lambda'} F_{\lambda'} \right) + \frac{1}{N_0} \sum_{\lambda' \lambda''}^{-} \frac{1}{2} \Gamma_{\lambda\lambda'\lambda''}^{(-)} \left(\xi_{\lambda\lambda''} F_{\lambda''} + \xi_{\lambda\lambda'} F_{\lambda'} \right) \\
& + \frac{1}{N_0} \sum_{\lambda' \lambda'' \lambda'''}^{(++)} \frac{1}{2} \Gamma_{\lambda\lambda'\lambda''\lambda'''}^{(++)} \left(\xi_{\lambda\lambda'''} F_{\lambda'''} - \xi_{\lambda\lambda'} F_{\lambda'} - \xi_{\lambda\lambda''} F_{\lambda''} \right) \\
& \frac{1}{N_0} \sum_{\lambda' \lambda'' \lambda'''}^{(+-)} \frac{1}{2} \Gamma_{\lambda\lambda'\lambda''\lambda'''}^{(+-)} \left(\xi_{\lambda\lambda'''} F_{\lambda'''} - \xi_{\lambda\lambda'} F_{\lambda'} + \xi_{\lambda\lambda''} F_{\lambda''} \right) \\
& \frac{1}{N_0} \sum_{\lambda' \lambda'' \lambda'''}^{(--)} \frac{1}{6} \Gamma_{\lambda\lambda'\lambda''\lambda'''}^{(--)} \left(\xi_{\lambda\lambda'''} F_{\lambda'''} + \xi_{\lambda\lambda'} F_{\lambda'} + \xi_{\lambda\lambda''} F_{\lambda''} \right) \\
& + \frac{1}{N_0} \sum_{\lambda'}^{(iso)} \Gamma_{\lambda\lambda'}^{(iso)} \xi_{\lambda\lambda'} F_{\lambda'}
\end{aligned}, \tag{2}$$

where the shorthand notation $\xi_{\lambda\lambda'} = \omega_{\lambda'} / \omega_\lambda$ with phonon frequency ω, N_0 denotes the total number of sampled phonon wavevectors in the first BZ. In Eq.(2), the superscripts (+-) or (++, +-, and --) represent the three- and four-phonon scatterings processes, satisfying $\boldsymbol{q}'' = \boldsymbol{q} \pm \boldsymbol{q}' + \boldsymbol{Q}$ and $\boldsymbol{q}''' = \boldsymbol{q} \pm \boldsymbol{q}' \pm \boldsymbol{q}'' + \boldsymbol{Q}$, respectively, where $\boldsymbol{Q}$ is the reciprocal lattice vector. *iso* is the abbreviation of the isotope. The scattering rate Γ then can be written as:

$$\Gamma^{(\pm)}_{\lambda\lambda'\lambda''}=\frac{\hbar\pi}{4}\frac{\begin{Bmatrix} n_{\lambda'}-n_{\lambda''} \\ n_{\lambda'}+n_{\lambda''}+1 \end{Bmatrix}}{\omega_\lambda\omega_{\lambda'}\omega_{\lambda''}}\left|V^{(\pm)}_{\lambda\lambda'\lambda''}\right|^2\delta\left(\omega_\lambda\pm\omega_{\lambda'}-\omega_{\lambda''}\right), \tag{3}$$

$$\Gamma^{\begin{pmatrix}++\\+-\\--\end{pmatrix}}_{\lambda\lambda'\lambda''\lambda'''}=\frac{\hbar^2\pi}{8N_0}\frac{\begin{Bmatrix}(1+n_{\lambda'})(1+n_{\lambda''})n_{\lambda'''} \\ (1+n_{\lambda'})n_{\lambda''}n_{\lambda'''} \\ n_{\lambda'}n_{\lambda''}n_{\lambda'''}\end{Bmatrix}}{n_\lambda}\left|V^{\begin{pmatrix}++\\+-\\--\end{pmatrix}}_{\lambda\lambda'\lambda''\lambda'''}\right|^2\frac{\delta\left(\omega_\lambda\begin{bmatrix}+\\+\\-\end{bmatrix}\omega_{\lambda'}\begin{bmatrix}+\\-\\-\end{bmatrix}\omega_{\lambda''}-\omega_{\lambda'''}\right)}{\omega_\lambda\omega_{\lambda'}\omega_{\lambda''}\omega_{\lambda'''}}, \tag{4}$$

where n and V denote phonon distribution function and cubic/quartic scattering matrix elements[36, 37], respectively. In Eq.(1), τ^0_λ represents the phonon relaxation time for a mode λ, which can be obtained from perturbation theory under the SMRTA. Using Matthiessen's rule, τ^0_λ can be defined as:

$$\begin{aligned}\frac{1}{\tau^0_\lambda}=&\frac{1}{N_0}\left(\sum^{(+)}_{\lambda'\lambda''}\Gamma^{(+)}_{\lambda\lambda'\lambda''}+\sum^{(-)}_{\lambda'\lambda''}\frac{1}{2}\Gamma^{(-)}_{\lambda\lambda'\lambda''}\right)+\frac{1}{N_0}\sum^{(iso)}_{\lambda'}\Gamma^{(iso)}_{\lambda\lambda'}\\&+\frac{1}{N_0}\left(\sum^{(++)}_{\lambda'\lambda''\lambda'''}\frac{1}{2}\Gamma^{(++)}_{\lambda\lambda'\lambda''\lambda'''}+\sum^{(+-)}_{\lambda'\lambda''\lambda'''}\frac{1}{2}\Gamma^{(+-)}_{\lambda\lambda'\lambda''\lambda'''}+\sum^{(--)}_{\lambda'\lambda''\lambda'''}\frac{1}{6}\Gamma^{(--)}_{\lambda\lambda'\lambda''\lambda'''}\right)\end{aligned}, \tag{5}$$

where $\Gamma_{\lambda\lambda'}$ denotes the isotopic impurity scattering rate associated with two phonons and it can be written as[41]:

$$\Gamma_{\lambda\lambda'}=\frac{\pi\omega^2}{2}\sum_{i\in u.c.}g(i)\left|e^*_\lambda(i)\cdot e_{\lambda'}(i)\right|^2\delta(\omega-\omega'), \tag{6}$$

where $g(i)$ and e_λ represent the mass variance and eigenvector, respectively.

Using the above determined $\boldsymbol{F}$, the tensor-dependent lattice thermal conductivity κ can be then calculated by:

$$\kappa^{\alpha\beta}=\frac{1}{k_BT^2\Omega N_0}\sum_\lambda n_0(n_0+1)(\hbar\omega_\lambda)^2\upsilon^\alpha_\lambda F^\beta_\lambda, \tag{7}$$

where Ω denotes the volume of the primitive cell, T denotes the Kelvin temperature, k_B denotes the Boltzmann constant, $\hbar$ denotes the Plank constant, and υ denotes the phonon group

velocity. The tensor directions are denoted respectively by α and β. In the current study, for three-phonon scattering processes, we solved the PBTE iteratively with a fine $\boldsymbol{q}$-point mesh of 28×28 ×28, whereas we treated the four-phonon scattering processes at SMRTA scheme using a coarse $\boldsymbol{q}$ mesh of $13\times13\times13$ considering the huge demand of computational memory and cost. It is worth noting that both $\boldsymbol{q}$-points mesh for different phonon-phonon scattering events already achieve well-converged results [see Figure. S1 in Supplementary material]. However, the lattice thermal conductivity κ computed by Eq.(7) considers only the diagonal contribution, recently, a unified theory of thermal transport accounting for both diagonal and nondiagonal contributions of heat flux operator was derived by Simoncelli *et al.*[24]. The detailed form of the lattice thermal conductivity κ including all contributions within the SMRTA scheme can be defined as:

$$\kappa = \frac{\hbar^2}{k_B T^2 \Omega N_0} \sum_{\boldsymbol{q}} \sum_{j,j'} \frac{\omega_{\boldsymbol{q}}^{j} + \omega_{\boldsymbol{q}}^{j'}}{2} \boldsymbol{\upsilon}_{\boldsymbol{q}}^{j,j'} \otimes \boldsymbol{\upsilon}_{\boldsymbol{q}}^{j',j} \frac{\omega_{\boldsymbol{q}}^{j} n_{\boldsymbol{q}}^{j}(n_{\boldsymbol{q}}^{j}+1) + \omega_{\boldsymbol{q}}^{j'} n_{\boldsymbol{q}}^{j'}(n_{\boldsymbol{q}}^{j'}+1)}{4(\omega_{\boldsymbol{q}}^{j} - \omega_{\boldsymbol{q}}^{j'})^2 + (\Gamma_{\boldsymbol{q}}^{j} + \Gamma_{\boldsymbol{q}}^{j'})^2} (\Gamma_{\boldsymbol{q}}^{j} + \Gamma_{\boldsymbol{q}}^{j'}) \quad (8)$$

where the interbranch generalization of phonon group velocity is defined as[42]:

$$\boldsymbol{\upsilon}_{\boldsymbol{q}}^{j',j} = \frac{< e_{\boldsymbol{q}}^{j} | \frac{\partial D(\boldsymbol{q})}{\partial \boldsymbol{q}} | e_{\boldsymbol{q}}^{j'} >}{2\sqrt{\omega_{\boldsymbol{q}}^{j} \omega_{\boldsymbol{q}}^{j'}}}, \quad (9)$$

where the dynamical matrix and polarization vector are denoted respectively by $D(\boldsymbol{q})$ and $e_{\boldsymbol{q}}^{j}$. If we consider only the diagonal terms, namely, $j = j'$, in heat flux operators, Eq.(8) can be reduced to the simple form of Eq.(7) and gives Peierls's contribution. Conversely, considering only the non-diagonal terms, i.e., $j \neq j'$, results in the coherence contributions.

3. **Results and discussion**

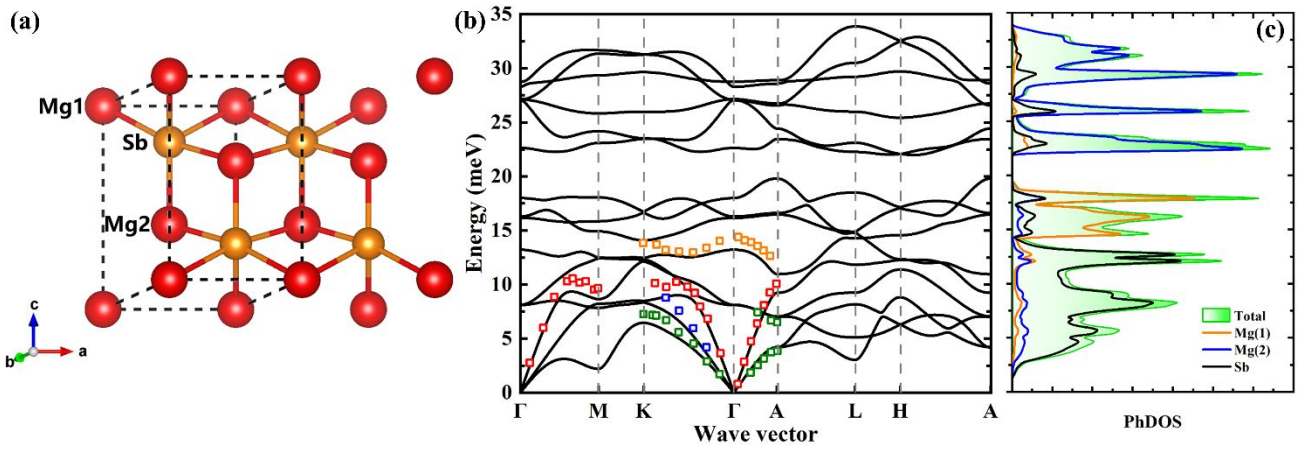

Fig. 1 (a) Crystal structure of layered Zintl-phase Mg_3Sb_2 (The corresponding Mg1 and Mg2 atoms generally expressed the Mg^{2+} and $[Mg_2Sb_2]^{2-}$ layers, respectively.). (b) Calculated phonon dispersions along the high-symmetry path in the BZ and (c) atom-projected densities of states (PhDOS) for Mg_3Sb_2 at 300 K. Inelastic X-ray scattering (IXS) experimental measurements data from Kanno *et al.*[43] are included (open square markers) and compared with DFT phonon dispersion.

The crystal structure of Mg_3Sb_2 is illustrated in Fig. 1(a), which belongs to the classical trigonal conventional cell (space group: $P\bar{3}m1$), and its layered structure can be described by the Mg^{2+} cationic layers (Mg1 is located on the octahedron site) and the bound $[Mg_2Sb_2]^{2-}$ anionic network layers (Mg2 is located on the tetrahedron site). The primitive cell of nanocrystalline Mg_3Sb_2 contains five atoms of which three Mg atoms are bonded to other two Sb atoms with lengths of 2.825, 2.937, and 3.083 Å, respectively. Using the DFT method, we optimized the lattice parameters of Mg_3Sb_2 and obtained values of a= 4.554 Å and c= 7.189 Å, and the experimental values[11] was a= 4.562 Å and c= 7.229 Å at 299 K. It is found that our calculation results agree well with the experiments for Mg_3Sb_2 single crystal. We next by discuss the calculated phonon vibrational properties (namely, the phonon dispersions and atom-projected densities of states) are presented in Figs. 1(b) and (c). Overall, there are not any imaginary phonon energy in the first BZ, which indicates that Mg_3Sb_2 structure is dynamically stable. Meanwhile, we find that the Mg1, Mg2, and Sb atoms have distinct

ranges of phonon vibrational energy, i.e., they mainly dominate the mid-, high-, and low-phonon energy ranges, respectively. This is because that Sb element has the heaviest atomic mass and therefore shows the slowest vibration. Both Mg1 and Mg2 atoms, owing to existing the two types of local bonding environment in Mg_3Sb_2, express that the former Mg atom bonded (Mg1-Sb) is much looser than that of the Mg2-Sb bonds, therefore Mg2 atom in the Mg_3Sb_2 lattice vibrate most rapidly. To better validate our theoretical calculations, we compare the theoretically predicted with the measured phonon dispersions of hypothetical perfect Mg_3Sb_2 crystal, as shown in Fig. 1(b). This is clearly seen that the general consistency between measured data from IXS and our computed phonon vibrational energy along the high-symmetry paths in the BZ (Γ-M, Γ-K, and Γ-A). In particular, the green, blue, and red open squares, corresponding to the fitted phonon energy at 300 K, are the two transverse phonon modes (labeled TA1 and TA2) and the longitudinal phonon mode (labeled LA), respectively. Notably, no band-gap between acoustic and optical phonons (Optical) in Mg_3Sb_2 will promote three-phonon scattering processes among acoustic- and optical-phonons, leading to a lower lattice thermal conductivity. More importantly, it has been investigated that the role of four-phonon scattering processes in some lower thermal conductivities solids can not be ignored[44], for instance, in CuCl (~1 $Wm^{-1}K^{-1}$)[45, 46], PbSe (~1.5 $Wm^{-1}K^{-1}$)[47], and PbTe (~2 $Wm^{-1}K^{-1}$)[47] at 300 K.

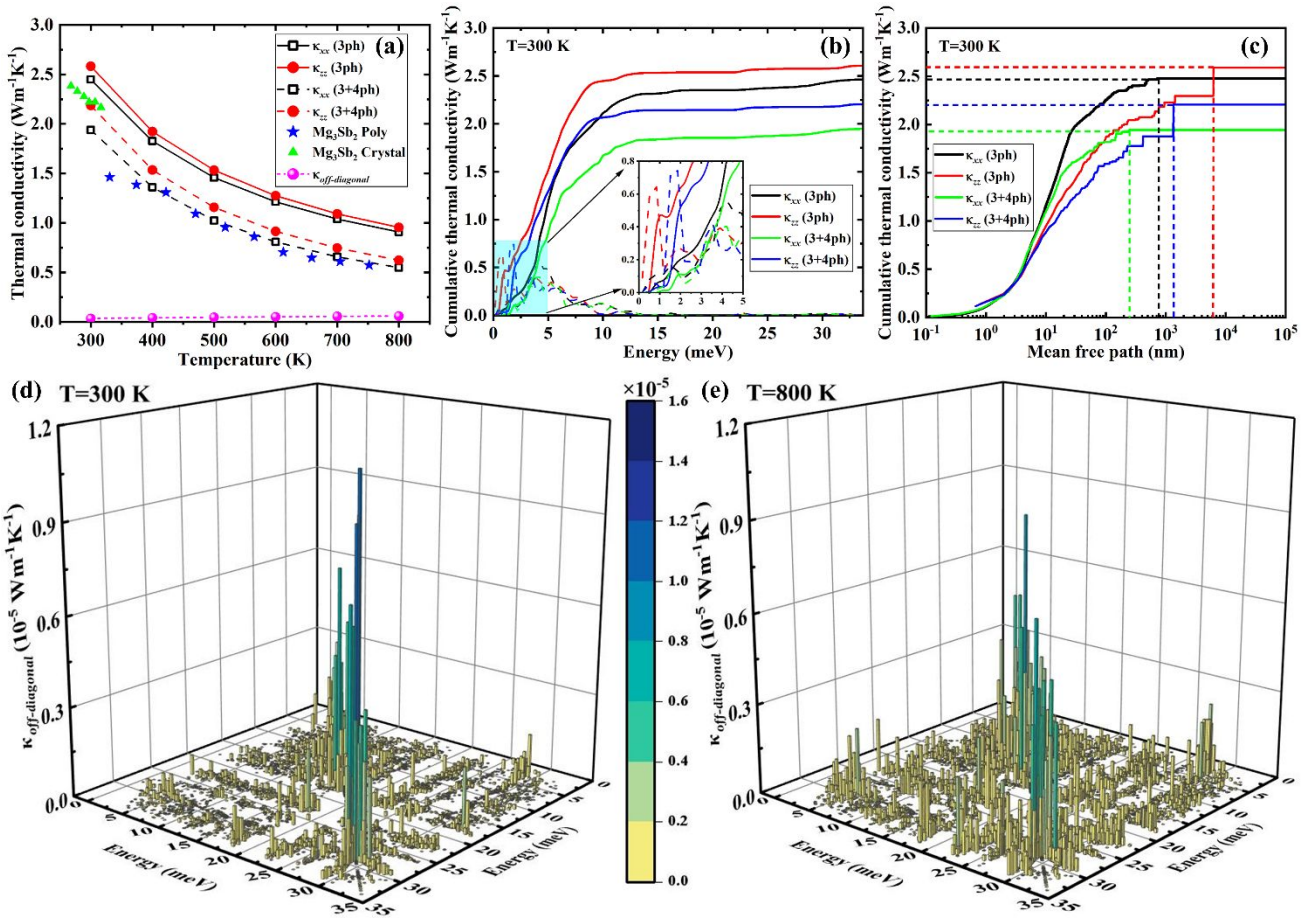

Fig. 2 (a) Temperature-dependent in-plane (*xx*) and cross-plane (*zz*) lattice thermal conductivities (κ) of nanocrystalline Mg_3Sb_2 without (3ph) and with four-phonon (3+4ph) scattering processes in comparison with experimental data from Refs[48, 49]. The purple sphere shows the ratio of κ from the off-diagonal parts ($\kappa_{off\text{-}diagonal}$) as a function of temperature. (b) Calculated cumulative (solid lines) and corresponding differential (dashed lines) κ along the *xx*- and *zz*-directions with 3ph and 3+4ph models *versus* phonon energy at 300 K. (c) Phonon mean free path-dependent cumulative κ along the *xx*- and *zz*-directions with 3ph and 3+4ph models in Mg_3Sb_2 at 300 K. Contour plots of the $\kappa_{off\text{-}diagonal}$ contribution to κ at 300 K (d) and 800 K (e) in Mg_3Sb_2 *versus* various pairs of phonon energy.

Herein, we study phonon thermal transport properties of nanocrystalline Mg_3Sb_2 associated with quartic anharmonicity effect. First, we calculate the κ of Mg_3Sb_2 and illustrate the corresponding results as a function of temperature from 300 K and 800 K, as shown in Fig. 2(a). Owing to its asymmetric crystal structure, the κ exists anisotropic and the calculated lattice thermal conductivities in both in- (κ_{xx}) and cross-plane (κ_{zz}) directions. Meanwhile, κ_{xx}(3ph) and κ_{zz}(3ph) are 2.45 $Wm^{-1}K^{-1}$

and 2.58 $Wm^{-1}K^{-1}$ at 300 K (corresponding convergence test in Figure S1, Supplementary Material), in good agreement with previous theoretical results[20]. By further considering 4ph scattering, κ_{xx}(3+4ph) and κ_{zz}(3+4ph) are 1.94 $Wm^{-1}K^{-1}$ and 2.19 $Wm^{-1}K^{-1}$ for Mg_3Sb_2 single crystal at same temperature [see in Fig. 2(a)], respectively. Obviously, the additional 4ph scattering bring about the reduction in the κ of ~20% over the entire temperature range compared with that computed by the lowest perturbation theory. It can be clearly seen that the effect of 4ph scattering is relatively smaller compared to Graphene[50, 51], cubic-BAs[52, 53], honeycomb-BAs[54] and θ-TaN[55] but still non-negligible. More importantly, our calculated κ at both directions with 4ph scattering effect matches very well with the measured data at several temperature points (blue pentagram and green triangle marked). This reveals the previous failure of the lowest perturbation theory in predicting the κ in nanocrystalline Mg_3Sb_2 and highlights the crucial role of higher-order phonon scattering. Additionally, Fig.2 (a) shows that the predicted κ_{zz}(3+4ph) at 300-400 K range are still higher than those of experimental data in Mg_3Sb_2 polycrystalline, which may be attributed to its intrinsic defects and disorder characteristics. Specially, we also calculate the temperature-dependent $\kappa_{off\text{-}diagonal}$ contribution from off-diagonal terms of the heat-flux operators[56] at the range of 300-800K using the unified theory proposed by Simoncelli *et al*.[24], as plotted in Fig. 2(a). The corresponding off-diagonal coupling of phonons vibrational energies as a function of temperature would further be studied in the following section, as illustrated in Figs. 2(d) and (e).

Meanwhile, to deeply reveal how 4ph scattering affects the κ of Mg_3Sb_2, we compare the energy cumulative computed κ without and with considering 4ph scattering and its derivative values at 300 K in Fig. 2(b). It can be clearly observed that both κ(3ph) and κ(3+4ph) from heat-carrying phonons have two energies centered at 3-5 meV and 0-2 meV (see the inset of Fig. 2(b)), respectively, which is corresponding to dispersive acoustic and the low-lying optical modes. We further find that, from the trends of κ(3ph) and κ(3+4ph) derivative in the above inset, the κ contributions from the modes with phonon energies larger than 5 meV would be significantly decreased, corresponding to all

acoustic phonons. It is worth noting that the κ(3ph) spectrum along cross-plane direction is lower than the κ(3+4ph) spectrum at same direction, which reveals the discrepancies between the experimental measurements and theoretical calculation data because of the overestimated contributions from 3ph processes. We next focus our attention on the corresponding mean free path (MFP) cumulative κ plotted in Fig. 2(c), to assess the κ and enhance thermoelectric performance by nanostructuring approach. It is apparent that from Fig. 2(c) that the inclusion of 4ph scattering in cumulative κ would remarkably reduce the maximum MFP (from 721.57 nm to 243.07 nm and 6218.19 nm to 1339.38 nm along in- and cross-plane directions at 300K, respectively), and significantly suppress heat transfer behavior from phonons with MFP larger than 2 nm. Interestingly, the above phenomenon is similar to the findings of β-GeTe[57] and HgTe[47] due to 4ph scattering influence, and producing nanostructures with sizes of Mg_3Sb_2 may efficiently reduce the κ. Moreover, to better elucidate the effect of 4ph scattering in Mg_3Sb_2, it is necessary to study the contributions of the off-diagonal terms to the total κ, especially in the lower κ systems[58-60]. Herein, we compare the contribution of the off-diagonal terms to κ at 300 K (see Fig. 2(d)) and 800 K (see Fig. 2(e)). According to the above discussion results, we know that calculated κ originates mainly from acoustic and the low-lying optical phonons, while all phonons spectrum of Mg_3Sb_2 contribute to the off-diagonal terms shown in Figs. 2(d) and (e). Obviously, the effect of the coherence terms on the contribution to κ in Mg_3Sb_2 would be strengthened by increasing temperature, as demonstrated before by Simoncelli *et al*.[24]. At 300 K, various pairs of phonon energy for the $\kappa_{off\text{-}diagonal}$ represents the coupling between quasi-degenerate states, while the $\kappa_{off\text{-}diagonal}$ at 800 K shows the inclusions of coupling the other phonons except the quasi-degenerate states phonons, which is mainly caused by the strong phonon anharmonicity.

Specially, the off-diagonal terms contribution in low-κ system is usually no longer negligible, while calculated the $\kappa_{off\text{-}diagonal}$ in Mg_3Sb_2 exists much smaller than the diagonal terms, because of its well-separated phonon modes (see Fig. 1(b)) and restraining wavelike tunneling in different phonon

vibrational eigenstates[47]. Besides, our results indicate that the effect of 4ph scattering in Mg_3Sb_2 is also crucial even at 300 K, which goes beyond the common theory (higher-order phonon scattering processes become noticeable at high temperature). To sum up, the above discussions unveil the lowest-order 3ph and the higher-order 4ph scattering processes effect in evaluating the κ of Mg_3Sb_2. To better elucidate the influence mechanism, we display phonon vibrational energy-dependent scattering rates by considering only with 3ph- and 4ph-scattering, as well as 3+4ph scattering processes and shown in Fig. 3. As plotted in Fig. 3(a), we note that the κ(3ph) along the two directions of Mg_3Sb_2 are significantly reduced from 2.45 to 1.94 $Wm^{-1}K^{-1}$ and 2.58 to 2.19 $Wm^{-1}K^{-1}$ at 300 K, respectively, upon including the 4ph scattering, while we note that 3ph scattering in Mg_3Sb_2 is still stronger than 4ph scattering in a large portion of phonon energy range. Meanwhile, it can be seen that the 4ph scattering rates in high-lying optical phonons are close to the corresponding 3ph scattering rates, which is consistent with recent studies that optical phonon modes are less affected by 4ph scattering[50, 61].

Most surprisingly, scattering rates of the acoustic phonons in Mg_3Sb_2 from 4ph interactions are quite strong, especially for phonon energy less than 5 meV. We next calculate the all phonons allowed phase space for 3ph- and 4ph-scattering processes and illustrated in Fig. 3(b). It is evident that the intrinsic κ of a material varies inversely with the phase space[40, 62], and the insets represent various types of 3ph- and 4ph-scattering diagrams, including the emission (λ-), absorption (λ+), splitting (λ--), redistribution (λ-+), and combination (λ++) processes. We note that the magnitude of λ-+ total phase space is close to those in λ- and λ+, indicating comparable strength effect from both 3ph scattering processes in phonon heat conduction. Moreover, to obtain more details about the above five individual scattering processes, we decompose and report the corresponding phonons mode-dependent scattering rates in Figs. 3(c) and (d). As plotted in Fig. 3(d), it is intriguing to see that the λ-+ process dominates over the λ--and λ++ processes in the entire energy range, which agrees with their scattering total phase space.

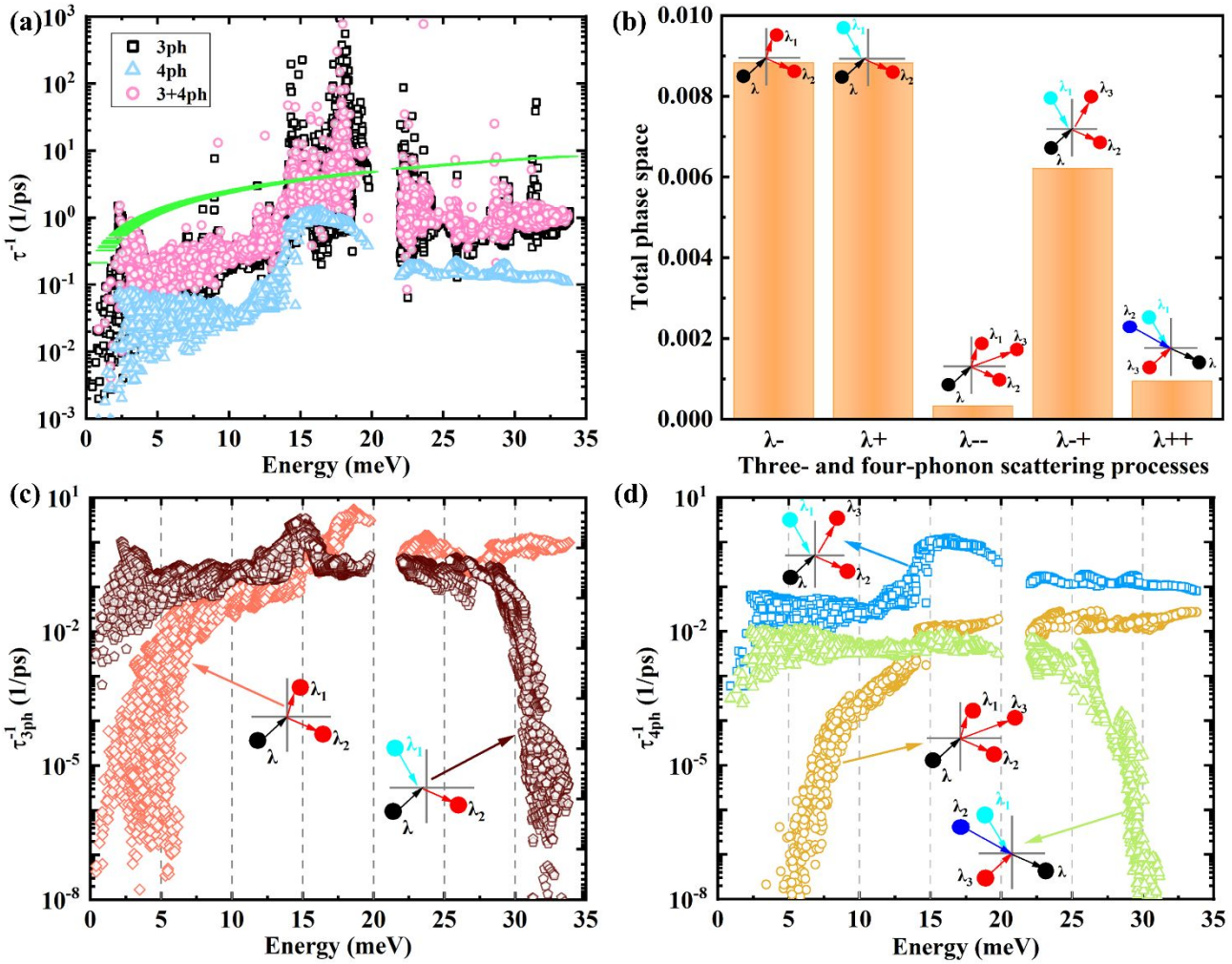

Fig. 3 (a) Comparison of the 3ph- and 3+4ph-scattering rates (τ^{-1}) in Mg_3Sb_2. The green line represents the τ^{-1} to be twice the phonon vibrational frequency, as employed in the Cahill model[63] to predict minimum κ. (b) Comparison of the total volume in phase space available for 3ph- and 3+4ph-scattering processes. In (c) and (d), the 3ph and 4ph scattering rates into are decomposed the emission ($\lambda \rightarrow \lambda_1 + \lambda_2$), absorption ($\lambda + \lambda_1 \rightarrow \lambda_2$), splitting ($\lambda \rightarrow \lambda_1 + \lambda_2 + \lambda_3$), redistribution ($\lambda + \lambda_1 \rightarrow \lambda_2 + \lambda_3$), and combination ($\lambda + \lambda_1 + \lambda_2 \rightarrow \lambda_3$) processes, which are represented by red, brown, yellow, blue, and green, respectively.

Indeed, the λ-+ processes have predominant contributions in 4ph-scattering, because of satisfying easily the energy conservation for all phonons[57] and thus contributing much more 4ph interaction parts. Compared to the classical 3ph-scattering processes behavior, 4ph-scattering processes have never been studied in bulk Mg_3Sb_2. To obtain deeper insight, we further decompose the overall scattering processes into the Normal and Umklapp processes, which can play an

important role for the theoretical prediction of κ[38], namely, 3ph-Normal, 4ph-Normal, 3ph-Umklapp, and 4ph-Umklapp processes as displayed in Figure S2 (see Supplementary material). It is worth noting that the Umklapp process dominates in total 3ph- and 4ph-scattering rates, which suggests that the relaxation time approximation results for the calculated κ for Mg_3Sb_2 is similarly equal to the iterative solution of the Boltzmann Transport Equation (BTE)[38, 64]. Meanwhile, the corresponding Born effective charge tensor and dielectric tensor in Mg_3Sb_2 were considered when solving BTE.

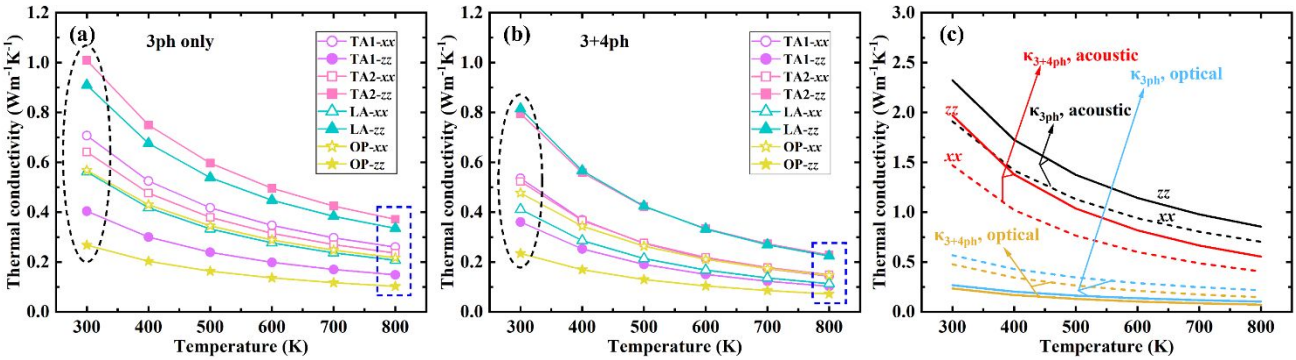

Fig. 4 Temperature–dependent κ of TA1, TA2, LA, and Optical (OP) modes for Mg_3Sb_2 without 4ph-scattering (a) and with 4ph-scattering (b) processes along the *xx*- and *zz*-directions. (c) The comparison between 3ph and 3+4ph contribution to κ from total acoustic and optical phonons as a function of temperature.

Herein, we also display the contribution of all phonons to κ without and with 4ph scattering at the two directions as a function of temperature, as illustrated in Fig. 4 and Table S1 (see Supplementary material). It can be seen from Figs. 4 (a) and (b) that with 4ph scattering included in Mg_3Sb_2, the OP contribution to κ along the *zz* direction in the range of 300-800 K exist less affected, which exhibits the same pattern in BAs predicted by Yang *et al.*[61]. This is mainly because of the lower splitting and combination scattering phase space of OP phonons in Mg_3Sb_2, which is mainly induced by the flatness trend of the optical modes. In addition, we note that the relative contribution from all OP phonons to our calculated κ at 300 and 800 K increase from 22.93% to 24.48% and 23.58% to 26.57% in the *xx* direction, respectively, after considering 4ph scattering. The phenomenon suggests the acoustic phonons remain the major carriers of heat for including higher-order phonon scattering processes in Mg_3Sb_2, while the OP contribution to κ can not be

neglected, especially in the higher-temperature ranges (the power law of 4ph scattering for OP phonons as $\tau_{4ph}^{-1} \sim T^2\omega^4$)[44, 65]. It is worthwhile to note that the total acoustic modes (TA1, TA2, and LA) contributions to κ exist little change, and we show in Fig. 4 (c) the effect of total acoustic and OP modes contributions to κ with and without 4ph scattering types with response to the different directions. By comparing our result of κ(3ph) and κ(3+4ph), we find that the relative contribution of 4ph scattering shows a weaker temperature dependence in Mg_3Sb_2.

To further estimate the significance of 4ph scattering, we study the *n*th-order IFC, namely, Φ_2 (eV/Å^2), Φ_3 (eV/Å^3), and Φ_4 (eV/Å^4) and as displayed in Fig. 5 and Table 1, which exists roughly proportional to the *n*th-order phonon scattering rates. As shown in Fig, 5 (a), the relative modulus of the 2nd IFC ($|\Phi_2|$) are examined and described with these bonds length. Specially, we note that the magnitude of $|\Phi_2|$ very strongly depends on the nearest-neighbor distance, for instance, 2.48 eV/Å^2 for 2.83 Å, 1.51 eV/Å^2 for 2.94 Å, and 0.53 eV/Å^2 and 3.08 Å in Mg_3Sb_2. Meanwhile, the $|\Phi_2|$ change trend in these bonds can be understood by the crystal orbital Hamiltonian population (COHP), which are computed with the Local Orbital Basis Suite towards Electronic-Structure Reconstruction (LOBSTER)[66]. Meanwhile, the ICOHP value is assumed to be the additive inverse of the integral of a "-pCOHP" curve to the whole energy range (defined as $\mathrm{ICOHP} = \int_{-\infty}^{E} \mathrm{pCOHP}(E)\,dE$). As seen in Fig. 5 (b), the IpCOHP value for d_1 represents similarly equal to d_2 and larger than d_3, which agrees well with the change of the corresponding $|\Phi_2|$ in Mg_3Sb_2. It is well known that the bond strength is a partial factor to determine the lattice thermal conductivity, and some atomic bonds predicted in novel carbon allotropes have been done by Yue *et al.*[67]. Therefore, we need further estimate higher-order IFC contribution to the κ.

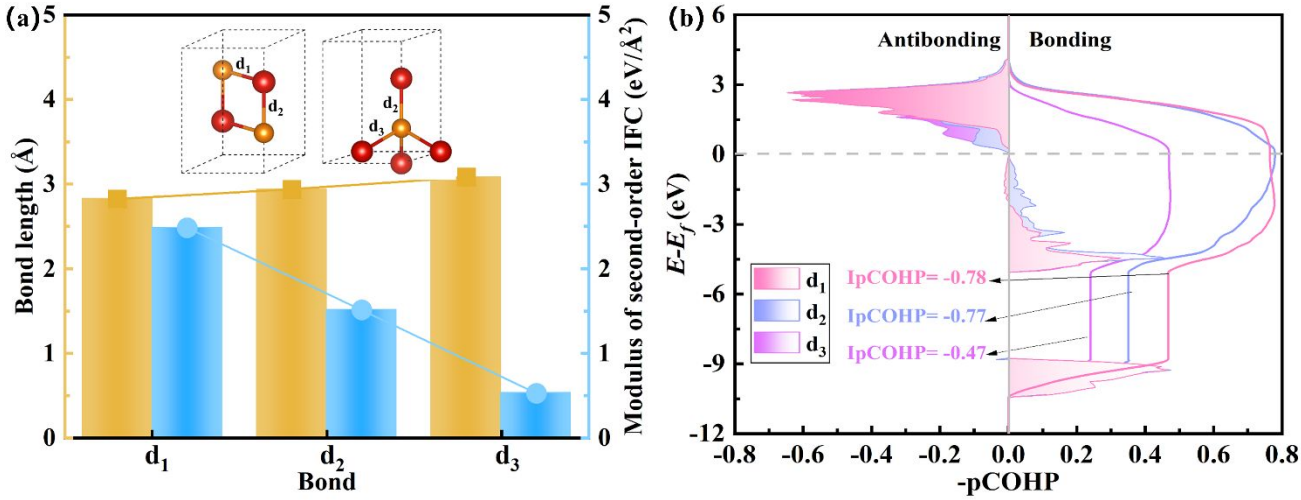

Fig. 5 (a) The three-types bonds between Mg and Sb atoms (d_1, d_2, and d_3) in Mg_3Sb_2 crystal are defined from the inset, and these bonds with respect to bond length and modulus of second-order interatomic force constant (IFC). (b) Energy with respect to the Fermi energy (E_f) *versus* pCOHP in Mg_3Sb_2. Herein, the left and right parts of the "-pCOHP" curves represent antibonding and bonding interactions, respectively. The large the absolute value of IpCOHP, the stronger bond strength.

Generally speaking, the *n*th-order scattering rate (τ_n^{-1}) exists following approximately $\tau_n^{-1} \sim |V_n|^2 f^{n-2} / \omega^{n+1}$ relationship, where V_n represents the *n*th-order transition matrix element ($V_n \sim \Phi_n / m^{n/2}$)[44]. Herein, Φ_n, m, and f denote the maximum value of the *n*th-order IFC, the average atomic mass, and phonon occupation number (obeying the Bose-Einstein distribution). Meanwhile, because phonon frequency (ω) can be expressed as $\omega \sim \sqrt{\Phi_2 / m}$, then the relationship of considering 4ph anharmonicity strength are defined as $\tau_4^{-1} / \tau_3^{-1} \sim |\Phi_4 / \Phi_3|^2 / |\Phi_2|$, and the relative results are listed in Table 1. Particularly, to better compare and quantify the importance of 4ph scattering in different lattice thermal conductivities, we choose CuCl (~1 $Wm^{-1}K^{-1}$ at 300 K)[45, 46] and common Si materials. Note that the value of $|\Phi_4 / \Phi_3|^2 / |\Phi_2|$ in Mg_3Sb_2 is much larger than in Si and the same order of magnitude for CuCl, which also indicates that 4ph scattering in lower κ systems are also very significant, expecting for ultra-high κ systems. Furthermore, the relatively large 4ph terms in corresponding Hamiltonians for some soft materials may be caused by atomic

deviating significantly at equilibrium position. This could be attributed to the fact that the phonon scattering matrix terms reduced leads to the change of higher-order anharmonicity IFCs, which is positively relevant to the total phonon scattering phase space. Finally, we guess that the impact of 4ph scattering may also be significant in other Zintl-phase thermoelectric compounds, such as Eu_2ZnSb_2[68] and $YbMg_2Sb_2$[69].

Table 1. Calculated higher-order lattice anharmonicity ratio $|\Phi_4 / \Phi_3|^2 / |\Phi_2|$ to approximately describe the relative importance of 4ph scattering in Mg_3Sb_2, CuCl[44], and Si[44, 70], respectively.

Material	$\|\Phi_2\|$	$\|\Phi_3\|$	$\|\Phi_4\|$	$\|\Phi_4 / \Phi_3\|^2 / \|\Phi_2\|$
Mg_3Sb_2	5.15	8.31	20.65	1.199
CuCl	1.93	13.10	48.00	6.956
Si	13.60	33.90	50.80	0.165

4. **Conclusion**

In conclusion, in nanocrystalline Mg_3Sb_2, we have systematically investigated the impact of 4ph scattering and the off-diagonal terms contributions to the κ on the lattice thermal transport properties at the studied temperatures using *ab-initio* calculations and a unified theory of lattice thermal transport approaches. We find that our calculated κ with considering 4ph effect successfully solve the divergence in theoretical predictions and experimental measurements in the previous excellent works, suggesting a stronger 4ph scattering process (redistribution), which is mainly caused by the unusual features (for instance, the bonding characteristic and the steepness of the optical phonons) in Mg_3Sb_2. Interestingly, our calculated $\kappa_{off\text{-}diagonal}$ coupling the particle-like propagation and wave-like tunneling of phonons show that the off-diagonal contributions along in (cross)-plane directions are not critical role, because of its large phonon interbranch-spacings. Furthermore, beyond the common sense, the 4ph scattering processes is strikingly important in ultra-low κ solid compounds, arising the predicted κ at 300 K in Mg_3Sb_2 from 2.45 (2.58) $Wm^{-1}K^{-1}$ to 1.94 (2.19) $Wm^{-1}K^{-1}$ at the two directions. Meanwhile, after considering the effect of higher-order 4ph scattering, we also find that the corresponding phonons contributing to the κ in both directions have an order of magnitude lower

MFP than that for the including only 3ph scattering case at 300 K in Mg_3Sb_2. Herein, it is reasonable to hazard a guess that our results are not special, and they most likely exist in other Zintl phase thermoelectric materials. On revisiting the κ with the inclusion of the off-diagonal terms and 4ph scattering case in Mg_3Sb_2, the obtained results from the microscopic understanding of lattice thermal transport mechanism, are expected to accelerate discovery of ultra-low κ compounds for broadening the thermoelectrics and thermal barrier coatings applications and then offer guidance towards designing various thermal/energy functional materials.

Supplementary materials

The corresponding data that supports the findings of the work are in the manuscripts and Supplementary material, which will be available upon reasonable request.

Declaration of competing interest

The authors declare no competing financial interests or personal relationships that could have appeared to influence the work reported in this paper.

Acknowledgments

This work was supported by the National Natural Science Foundation of China [Grants Nos. 51720105007, 52076031, 11602149, 51806031, and 52176166] and the Fundamental Research Funds for the Central Universities [DUT19RC(3)006], and the computing resources from the Supercomputer Center of Dalian University of Technology. Research reported in this publication was supported in part by the U.S. National Science Foundation [Grants No. 1905775 and No. 2030128]. We are also thankful for the fruitful discussions with Prof. Guangzhao Qin and Dr. Linfeng Yu from Hunan University.

References

1. B. Wang, L. He, X.-C. Yuan, Z.-M. Sun and P. Liu, *Journal of Cleaner Production*, 2021, **295**, 126377.
2. J. He and T. M. Tritt, *Science*, 2017, **357**, eaak9997.
3. Z. Chang, K. Liu, Z. Sun, K. Yuan, S. Cheng, Y. Gao, X. Zhang, C. Shen, H. Zhang and N. Wang, *International Journal of Extreme Manufacturing*, 2022, **4**, 025001.
4. Y. Ouyang, Z. Zhang, D. Li, J. Chen and G. Zhang, *Annalen der Physik*, 2019, **531**, 1800437.
5. Z. Chang, K. Yuan, Z. Sun, X. Zhang, Y. Gao, G. Qin and D. Tang, *Physical Chemistry Chemical Physics*, 2021, **23**, 13633-13646.
6. H. Tamaki, H. K. Sato and T. Kanno, *Advanced Materials*, 2016, **28**, 10182-10187.
7. S. Ohno, K. Imasato, S. Anand, H. Tamaki, S. D. Kang, P. Gorai, H. K. Sato, E. S. Toberer, T. Kanno and G. J. Snyder, *Joule*, 2018, **2**, 141-154.
8. K. Imasato, S. Ohno, S. D. Kang and G. J. Snyder, *APL Materials*, 2018, **6**, 016106.
9. J. Mao, Y. Wu, S. Song, J. Shuai, Z. Liu, Y. Pei and Z. Ren, *Materials Today Physics*, 2017, **3**, 1-6.
10. F. Zhang, C. Chen, H. Yao, F. Bai, L. Yin, X. Li, S. Li, W. Xue, Y. Wang and F. Cao, *Advanced Functional Materials*, 2020, **30**, 1906143.
11. J. Zhang, L. Song, M. Sist, K. Tolborg and B. B. Iversen, *Nature communications*, 2018, **9**, 1-10.
12. K. Imasato, S. D. Kang, S. Ohno and G. J. Snyder, *Materials Horizons*, 2018, **5**, 59-64.
13. S. Kim, C. Kim, Y.-K. Hong, T. Onimaru, K. Suekuni, T. Takabatake and M.-H. Jung, *Journal of Materials Chemistry A*, 2014, **2**, 12311-12316.
14. J. Xin, G. Li, G. Auffermann, H. Borrmann, W. Schnelle, J. Gooth, X. Zhao, T. Zhu, C. Felser and C. Fu, *Materials Today Physics*, 2018, **7**, 61-68.

15. W. Peng, G. Petretto, G.-M. Rignanese, G. Hautier and A. Zevalkink, *Joule*, 2018, **2**, 1879-1893.

16. J. Mao, Y. Wu, S. Song, Q. Zhu, J. Shuai, Z. Liu, Y. Pei and Z. Ren, *ACS Energy Letters*, 2017, **2**, 2245-2250.

17. J. Shuai, B. Ge, J. Mao, S. Song, Y. Wang and Z. Ren, *Journal of the American Chemical Society*, 2018, **140**, 1910-1915.

18. M. B. Maccioni, R. Farris and V. Fiorentini, *Physical Review B*, 2018, **98**, 220301.

19. F. Meng, S. Sun, J. Ma, C. Chronister, J. He and W. Li, *Materials Today Physics*, 2020, **13**, 100217.

20. Y. Zhu, Y. Xia, Y. Wang, Y. Sheng, J. Yang, C. Fu, A. Li, T. Zhu, J. Luo and C. Wolverton, *Research*, 2020, **2020**.

21. O. Hellman, I. Abrikosov and S. Simak, *Physical Review B*, 2011, **84**, 180301.

22. O. Hellman and I. A. Abrikosov, *Physical Review B*, 2013, **88**, 144301.

23. Y. Xia, V. Ozoliņš and C. Wolverton, *Physical review letters*, 2020, **125**, 085901.

24. M. Simoncelli, N. Marzari and F. Mauri, *Nature Physics*, 2019, **15**, 809-813.

25. H. J. Cho, G. Kim, T. Onozato, H. Jeen and H. Ohta, *International journal of heat and mass transfer*, 2019, **137**, 263-267.

26. M. Hematiyan, A. Khosravifard and Y. Shiah, *International Journal of Heat and Mass Transfer*, 2015, **89**, 685-693.

27. P. Hohenberg and W. Kohn, *Physical review*, 1964, **136**, B864.

28. G. Kresse and J. Hafner, *Physical review B*, 1993, **47**, 558.

29. G. Kresse and J. Furthmüller, *Physical review B*, 1996, **54**, 11169.

30. P. Bliichl, *Phys Rev B*, 1994, **50**, 17953-17979.

31. J. P. Perdew, K. Burke and M. Ernzerhof, *Physical review letters*, 1996, **77**, 3865.

32. J. P. Perdew, A. Ruzsinszky, G. I. Csonka, O. A. Vydrov, G. E. Scuseria, L. A. Constantin, X. Zhou and K. Burke, *Physical review letters*, 2008, **100**, 136406.

33. R. Peierls and R. E. Peierls, *Quantum theory of solids*, Oxford University Press, 1955.

34. J. M. Ziman, *Electrons and Phonons: Theorz of Transport Phenomena in Solids*, Clarendon Press, 1962.

35. E. J. Candès and M. B. Wakin, *IEEE signal processing magazine*, 2008, **25**, 21-30.

36. W. Li, J. Carrete, N. A. Katcho and N. Mingo, *Computer Physics Communications*, 2014, **185**, 1747-1758.

37. Z. Han, X. Yang, W. Li, T. Feng and X. Ruan, *Computer Physics Communications*, 2022, **270**, 108179.

38. M. Omini and A. Sparavigna, *Physica B: Condensed Matter*, 1995, **212**, 101-112.

39. A. Ward and D. Broido, *Physical Review B*, 2010, **81**, 085205.

40. L. Lindsay and D. Broido, *Journal of Physics: Condensed Matter*, 2008, **20**, 165209.

41. S.-i. Tamura, *Physical Review B*, 1983, **27**, 858.

42. P. B. Allen and J. L. Feldman, *Physical Review B*, 1993, **48**, 12581.

43. T. Kanno, H. Tamaki, M. Yoshiya, H. Uchiyama, S. Maki, M. Takata and Y. Miyazaki, *Advanced Functional Materials*, 2021, **31**, 2008469.

44. T. Feng, L. Lindsay and X. Ruan, *Physical Review B*, 2017, **96**, 161201.

45. S. Mukhopadhyay, D. Bansal, O. Delaire, D. Perrodin, E. Bourret-Courchesne, D. J. Singh and L. Lindsay, *Physical Review B*, 2017, **96**, 100301.

46. G. A. Slack and P. Andersson, *Physical Review B*, 1982, **26**, 1873.

47. Y. Xia, V. I. Hegde, K. Pal, X. Hua, D. Gaines, S. Patel, J. He, M. Aykol and C. Wolverton, *Physical*

Review X, 2020, **10**, 041029.

48. J. Ding, T. Lanigan-Atkins, M. Calderón-Cueva, A. Banerjee, D. L. Abernathy, A. Said, A. Zevalkink and O. Delaire, *Science advances*, 2021, **7**, eabg1449.

49. J. Zhang, L. Song and B. B. Iversen, *npj Computational Materials*, 2019, **5**, 1-17.

50. T. Feng and X. Ruan, *Physical Review B*, 2018, **97**, 045202.

51. X. Gu, Z. Fan, H. Bao and C. Zhao, *Physical Review B*, 2019, **100**, 064306.

52. N. K. Ravichandran and D. Broido, *Physical Review X*, 2020, **10**, 021063.

53. Y. Ouyang, C. Yu, J. He, P. Jiang, W. Ren and J. Chen, *Physical Review B*, 2022, **105**, 115202.

54. C. Yu, Y. Hu, J. He, S. Lu, D. Li and J. Chen, *Applied Physics Letters*, 2022, **120**, 132201.

55. A. Kundu, X. Yang, J. Ma, T. Feng, J. Carrete, X. Ruan, G. K. Madsen and W. Li, *Physical Review Letters*, 2021, **126**, 115901.

56. R. J. Hardy, *Physical Review*, 1963, **132**, 168.

57. Y. Xia and M. K. Chan, *Applied Physics Letters*, 2018, **113**, 193902.

58. Y. Luo, X. Yang, T. Feng, J. Wang and X. Ruan, *Nature communications*, 2020, **11**, 1-10.

59. Q. D. Gibson, T. Zhao, L. M. Daniels, H. C. Walker, R. Daou, S. Hébert, M. Zanella, M. S. Dyer, J. B. Claridge and B. Slater, *Science*, 2021, **373**, 1017-1022.

60. Z. Zhang, Y. Guo, M. Bescond, J. Chen, M. Nomura and S. Volz, *Physical Review Letters*, 2022, **128**, 015901.

61. X. Yang, T. Feng, J. Li and X. Ruan, *Physical Review B*, 2019, **100**, 245203.

62. J. M. Ziman, *Electrons and phonons: the theory of transport phenomena in solids*, Oxford university press, 2001.

63. D. G. Cahill, S. K. Watson and R. O. Pohl, *Physical Review B*, 1992, **46**, 6131.

64. D. A. Broido, M. Malorny, G. Birner, N. Mingo and D. Stewart, *Applied Physics Letters*, 2007, **91**, 231922.

65. L. Xie, J. Feng, R. Li and J. He, *Physical Review Letters*, 2020, **125**, 245901.

66. R. Nelson, C. Ertural, J. George, V. L. Deringer, G. Hautier and R. Dronskowski, *Journal of Computational Chemistry*, 2020, **41**, 1931-1940.

67. S.-Y. Yue, G. Qin, X. Zhang, X. Sheng, G. Su and M. Hu, *Physical Review B*, 2017, **95**, 085207.

68. C. Chen, W. Xue, S. Li, Z. Zhang, X. Li, X. Wang, Y. Liu, J. Sui, X. Liu and F. Cao, *Proceedings of the National Academy of Sciences*, 2019, **116**, 2831-2836.

69. T. Zhou, Z. Feng, J. Mao, J. Jiang, H. Zhu, D. J. Singh, C. Wang and Z. Ren, *Chemistry of Materials*, 2020, **32**, 776-784.

70. X. Gu, S. Li and H. Bao, *International Journal of Heat and Mass Transfer*, 2020, **160**, 120165.